Spin dynamics of dense alkali-metal atoms

Kiyoshi Ishikawa,* Togo Kojima, Taro Hasegawa, and Yoshihiro Takagi
Department of Materials Science, Himeji Institute of Technology, Akogun, Hyogo 678-1297, Japan
(Received 15 August 2001; revised manuscript received 14 November 2001; published 20 February 2002)

The free induction signals of dense Rb atoms are observed with an injection-seeded power laser diode. The decay rate of signals is found to depend on the number density of Rb atoms, the static magnetic field, the electron spin polarization, and the pulse area of the oscillating magnetic field. We note that the observed broadening of the magnetic resonance line, appearing at high polarization and large pulse area, is the key to understanding the spin dynamics of the precessing atoms which interact with each other. The feature of broadening is quantitatively interpreted by numerically calculating, in a wide range of parameters, the nonlinear Liouville equation that includes the spin-exchange interaction between Rb atoms.

DOI: 10.1103/PhysRevA.65.032511 PACS number(s): 32.70.Jz, 32.80.Bx, 32.30.Dx,34.10.+x

I. INTRODUCTION

The alkali-metal atom in a glass cell is one of the familiar atoms used in spectroscopic studies. High-density alkali-metal atoms have gained extensive applications such as the polarization of noble-gas atoms for medical imaging, as a polarized target in high-energy physics, and in the NMR of spin-transferred atoms [1]. Recently it was demonstrated that the group velocity of a light pulse can be reduced to zero in dense Rb vapor in a glass cell [2]. To prolong the atomic coherence time for storing light information, it is important to study the spin dynamics of dense atoms. There are a number of studies on the spin behavior of optically polarized atoms [3] such as longitudinal spin relaxation slowed by the spin-exchange interaction [4–8], spin exchange with other species [9–11], and spin relaxation due to the alkali-metal dimers [12,13]. The line narrowing of dense atoms by spin-exchange interaction [14] is the pioneering work, and the study of polarized atoms in a pressurized noble gas [15] is the experimentally and theoretically comprehensive work related to this paper. These works were, however, performed under the condition of low polarization or weak rf field where an analytical solution can be obtained. In previous work on dense Rb atoms [16], we found that the decay time of the free induction (FI) signal depends on the rf pulse area, and that the amplitude of the spin echo decreases at large pulse area. The results could not be explained by the approximation of low polarization or weak rf field for the multilevel atom. If such a spin dynamics of dense atoms is quantitatively interpreted, we can measure the diffusion of atoms interacting with each other near the surface where the electric and magnetic fields affect the spin behavior [17,18].

The broadening of the magnetic resonance line derived from the FI signal, presented in the experimental results, is not caused by intense rf and light fields because FI signals are detected after turning off these fields except for a weak probe light. Around the magnetic field of 10 G, the linewidth of polarized atoms at high density and with large pulse area is broader than that at low polarization. Since the remarkable application of dense polarized atoms is spin transfer to other atoms such as noble-gas atoms, it is important to reduce the longitudinal decay rate. This is one of the reasons why the strange behavior of precessing spins has not been studied by solving the nonlinear Liouville equation.

In this paper we present the spin dynamics of dense alkali-metal atoms caused by the spin-exchange interaction. The decay rate of FI signals was observed to depend on various experimental parameters: the number density of Rb atoms N_{Rb}, the static magnetic field B_0, the electron spin polarization P, and the rf pulse area θ. In contrast to the case of low temperature, the rate was found to depend drastically on B_0, P, and θ at high temperature. In order to study this feature of the precessing spin of dense atoms, we introduce the spin interaction between Rb atoms in the Liouville equation as in previous work [7,14,15]. In the interaction term of a like-atom collision, the density operator appears nonlinearly. Because of the difficulty in analytically solving the nonlinear equation for a wide range of parameters, FI profiles of the Rb ground state are numerically obtained without a linear approximation. As a result of numerical integration of the Liouville equation, the time evolution of Zeeman coherence is quantitatively interpreted by the spin exchange interaction between Rb atoms. As the spin-exchange is the interaction known to dephase the coherence as well as to induce line narrowing of polarized atoms, we study the effect of the spin-exchange interaction, as a whole, on the spin dynamics of dense atoms. Details of the calculation and its coding for a computer program are described in the Appendixes.

II. EXPERIMENT

We observed FI signals of Rb atoms optically pumped with an injection-seeded high-power laser diode. In many experiments such as the optical polarization of the nuclear spin of noble-gas atoms, a high-power laser diode is used to pump the dense alkali-metal atoms. The linewidth of the free-running laser diode is, however, several nanometers. This is so broad that the optical pumping of alkali-metal atoms is not effective unless the buffer gas pressure and the cell temperature are controlled to match the atomic linewidth to the laser bandwidth. The spin relaxation time is shortened under this condition. Therefore the narrowing of the high-power laser diode is an effective way to polarize dense

*Electronic address: ishikawa@sci.himeji-tech.ac.jp

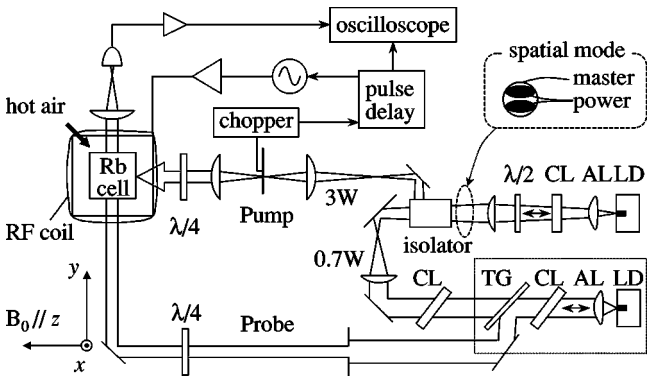

FIG. 1. Experimental setup to observe FI signal with master and power lasers. The power laser is seeded by the output of the master laser with the external grating. The spatial modes of master and power lasers at the optical isolator are schematically shown in the inset. LD is the laser diode, TG the transmission grating, CL a cylindrical lens, and AL an aspheric lens. The transmission of the probe beam is detected by an avalanche photodiode, whose output voltage is averaged by the digital oscilloscope.

alkali-metal atoms. There are many techniques for narrowing the power laser diode [19–26]. We used a combination of an external cavity diode as master laser and an injection-seeded power laser to pump Rb atoms. Injection seeding is a practical method to obtain the same frequency from the array of emitters in a high-power laser diode.

A. Power laser diode

The master laser is a single-stripe diode laser [27] with the external cavity shown in Fig. 1, which consists of an aspheric lens ($f=4.5$ mm), a cylindrical lens (15 mm), and a transmission grating (1800 lines/mm) in Littrow configuration. The cavity length is approximately 35 mm. There are four beams obtained from the output grating. The zeroth-order transmission is the main output of the master laser at 80% of the incoming intensity. The zeroth-order reflection (1%) is used as the probe beam. The first-order reflection (3%) is fed back to the laser diode. This weak reflection is enough for the narrowing if we monitor the two-dimensional image of the first-order transmission (0.5%) as it depends on the position of the emitter and the oscillation wavelength. For example, the oscillation wavelength depends on the position of the broad-area emitter if the cavity length is misaligned. We compared various gratings to obtain the best conditions in the reflectivity and dispersion. The reflection gratings make it easy to align the external cavity, but we could not find a noticeable refinement of the linewidth. The angle of the transmission grating, the temperature, and the electric current of the laser diode should be carefully controlled for tuning of both modes of the laser diode and external cavity to the Rb D_1 line. There are, however, advantages in using the transmission grating. The first one is that we can align any optics at the operating current without accidental feedback to destroy the laser diode. The second is that the intense output can be obtained within safety constraints. The third is that the optical path of the output is insensitive to the alignment of the grating in the Littrow configuration.

The above-mentioned advantages make it easy to inject the output of the master laser into the power laser of the double-stripe emitter [28]. It is hard to make a perfect match of spatial modes between the master and power laser beams. Thus we used a single aspheric lens (6.2 mm) in front of the power laser. The overlapping of beams is schematically shown in the inset of Fig. 1. The single stage of optical isolation at -30 dB is enough to avoid the coupling of lasers for our system. A Faraday isolator was also used to pick up the amplified laser beam. The spectrum of the free-running power laser is asymmetrically broadened near the D_1 line, originating from the unseparated lines of independent emitters. We could see a sharp line when the power laser was seeded, which indicates that the master laser is well injected to both emitters. The linewidth of the seeded power laser was estimated to be 46 GHz by measuring the line shape of pressure-broadened absorption of Rb atoms at 100 °C sealed with He gas at 97 kPa in a glass cell.

B. Free induction decay

The pump beam coming from the power laser was circularly polarized and propagated along the z axis, as shown in Fig. 1. The pulse width of pump light was typically 250 μs shaped by a mechanical chopper. The collision rate was so high in dense Rb atoms that the local spin temperature was established within the pulse duration. The circularly polarized probe beam came from the master laser along the y axis, and was continuously irradiated on the glass cell ($22\times22\times22$ mm^3) which was filled with Rb metal, ^{4}He (90 kPa), and N_2 (5 kPa) at room temperature. The cell temperature T was controlled by blowing hot air and varied between 60 °C and 120 °C. We estimated the density N_{Rb} from the vapor pressure at T [29]. The density is the most ambiguous one of the parameters controllable in our experiment. It is, however, important in this paper to point out how the linewidth of dense atoms depends on the pulse area and the polarization around $B_0=10$ G. Therefore, we leave the detailed consideration of the determination of atom density.

The rf pulse consisted of 5–7 cycles at defined phase of various frequencies from 90 kHz to 5 MHz, and was applied to the Rb cell by a two-turn coil driven by a 100 W amplifier. The coil is large enough to produce a homogenous magnetic field, and its Q value is so low that we can apply the rectangular envelope of the rf pulse to obtain the pulse area definitely. The transmission of the probe light was detected by an avalanche photodiode. The amplified signal was typically averaged over 500 times by a digital oscilloscope. Figure 2 shows the pulse sequence and a raw FI signal oscillating at Larmor frequency. In the analog system we used no narrowband filters distorting the amplitude and phase. After digitizing, every signal was processed with a computer as the digital filter and frequency converter. In the following analysis, we neglect the side effects of strong absorption, that Rb atoms are inhomogeneously pumped in the glass cell, and that the optically detected FI signal is distorted by saturation.

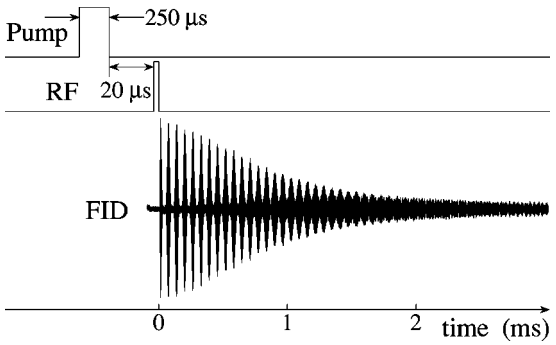

FIG. 2. Pulse sequence to obtain FI signals. The pump pulse is shaped by a mechanical chopper. The rf pulse is delayed by 20 μs from the end of the pump pulse. The FI decay (FID) is observed by monitoring the transmission of cw probe light. These are not on the same time scale.

III. RESULTS

Figure 3 shows the observed FI signals induced by the rf field of various pulse areas θ. The frequency of amplitude modulation is equal to the difference of Zeeman frequencies, and the modulation depth depends on the number of related transitions. The signal induced by the smaller θ has the longer decay time. The θ dependence of the decay time was absent at low temperature or low polarization. It is convenient for more analysis that we convert FI signals to Zeeman spectra by Fourier transform (FT) as shown in Fig. 4. There is a sharp line at $\theta=0.025\pi$ originating from the pumped level $|M_F=F\rangle$. The broad transitions at $\theta=\pi/2$ are resolved into large lines for the hyperfine levels $|F=3\rangle$ and small lines for $|F=2\rangle$. These are much broader than the line at $\theta=0.025\pi$. We could select the dependence of the linewidth on rf intensity from the rf power broadening by detecting the free precession. Since the rf pulse inducing the precession of ^{85}Rb atoms consists of only several cycles, the detuning of each Zeeman transition can be neglected, compared with the bandwidth of the rf spectrum. For ^{87}Rb atoms the rf field is almost off resonant, and its spin stays along the z axis. As shown in Fig. 5, we confirmed that no artifacts such as the distortion of the line shape, the decrease of the signal amplitude, and the phase shift of the precession appear in FI signals induced by a short rf pulse at any θ value. The resonance lines are unresolved because the Zeeman splitting at $B_0=2.7$ G is of the same order as the broadening at $T=118\,^{\circ}$C. We can see the θ dependence of the FT line shape and frequency, whose 2π period is explained by the periodicity of $d^K_{Q0}(\theta)$ in Eq. (A7).

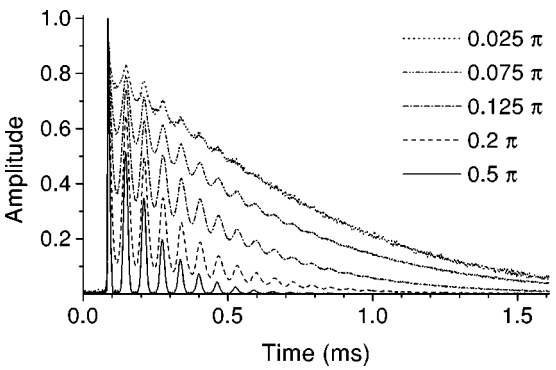

FIG. 3. The normalized envelopes of FI signals at various pulse areas θ, observed at $B_0=10.5$ G. $I_P=1$ W, $T=110\,^{\circ}$C. These envelopes are obtained from the in-phase and out-of-phase signals of digital phase-sensitive detection.

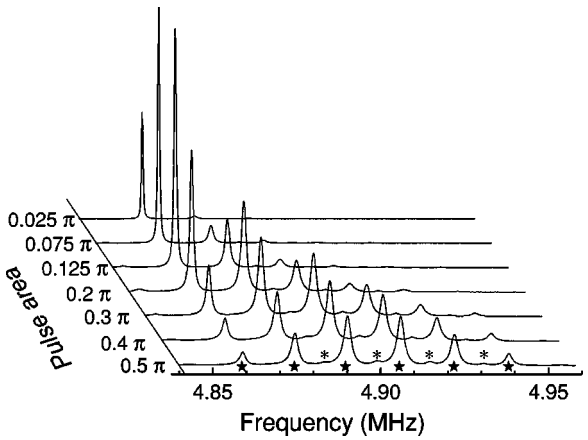

FIG. 4. Zeeman spectra obtained by Fourier transform of the FI signal shown in Fig. 3. The stars indicate the line for $|F=3\rangle$, the asterisks for $|F=2\rangle$.

In the analysis of linewidth, we fitted Lorentzian curves to the FT spectrum obtained experimentally or theoretically. For simplicity we use the same width for a single set of the parameters that characterize the spin dynamics of Rb atoms as follows.

Number density N_{Rb}. The decay rate of the FI signal increases at high temperature. The density of Rb atoms depends drastically on the temperature [29], but the mean velocity and cross section of collisions change slightly. The relaxation due to the buffer gas and wall collisions is less effective on the T dependence of the linewidth, although the pressure broadening of Zeeman transitions is dominant at low temperature. Therefore, the T dependence of the linewidth is caused by the Rb density changing the collision rate between Rb atoms.

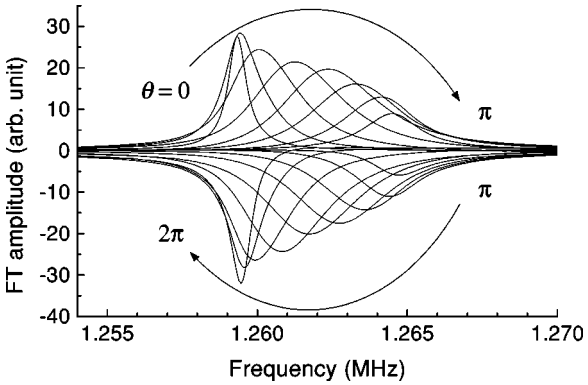

FIG. 5. The observed FT spectra depending on the pulse area θ at $B_0=2.7$ G, $I_P=1$ W, and $T=118\,^{\circ}$C. Zeeman transitions overlap in the linewidth. The rf pulse is taken over five cycles from a 1.262 MHz oscillator.

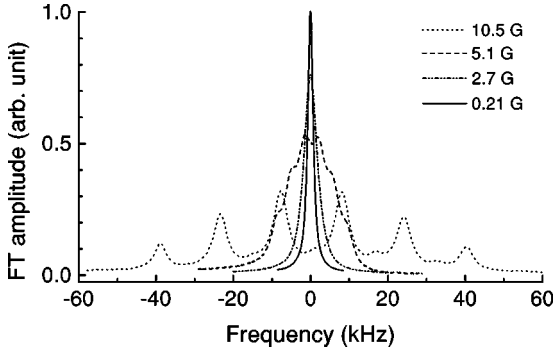

FIG. 6. The observed FT spectra at various magnetic fields B_0 at $I_P=1$ W, $T=110\,^{\circ}$C, and $\theta=\pi/2$. The frequency is measured from the center of the resonance lines.

Magnetic field B_0. The FT linewidth for $B_0=10$ G was broader than that for 0.2 G for dense Rb atoms as shown in Fig. 6. This seems contrary to the fact that the spin relaxation rate of gaseous atoms is generally decreased by increased B_0 because the Larmor frequency moves out of the spectrum of effective field fluctuations by the collisions. For the alkali-metal atoms in a noble gas at atmospheric pressure, the B_0 dependence of the relaxation rate due to the fluctuating perturbation is very slight in the range of B_0 in our experiment [3]. As described below, the broadening is due to the splitting of Zeeman frequencies, i.e., the modulation of coherences $\rho^1_{\pm 1}$.

Polarization P. Figure 7 shows the pump-power I_P dependence of FT spectra at small θ. The initial polarization was determined by the power I_P. There are broad resonance lines from the Zeeman transition caused by weak pumping, i.e., at small P. On the other hand, we can see a narrow line at large P. This is consistent with the line narrowing of the cw magnetic resonance of alkali-metal atoms in a noble gas [10]. Except for the strong relaxation due to the nuclear spin of noble-gas atoms, those results correspond to our experiment at large P and small θ. At large θ, the linewidth weakly depends on P and is rather broader at large P than at small P around $B_0=10$ G, as described below.

rf pulse area θ. In addition to the remarkable θ dependence of the FT linewidth shown in Fig. 4, it is noted that the

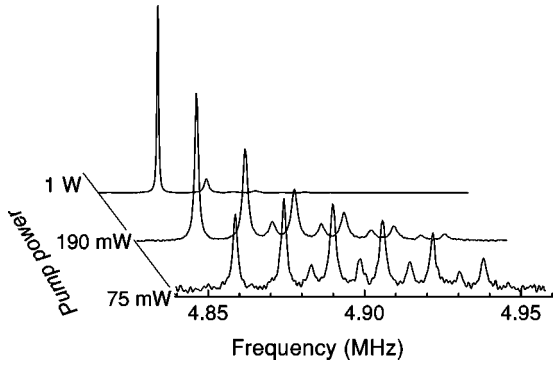

FIG. 7. Pump power dependence of the observed FT spectrum at $B_0=10.5$ G, $T=110\,^{\circ}$C, and $\theta=0.075\pi$. The amplitude of each spectrum is not to scale.

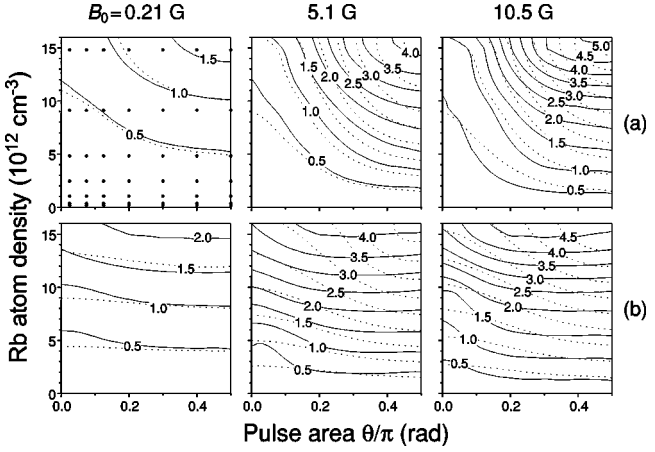

FIG. 8. The contour map of FT linewidth at various values of B_0, N_{Rb}, and θ. The solid lines are the linewidths observed at (a) $I_P=1$ W and (b) $I_P=190$ mW. The dashed lines are calculated at (a) $P=0.9$ and (b) $P=0.45$. The FI signals were observed at the points indicated by the solid circles in the left column of row (a), where the atom densities are obtained from the temperatures 118, 110, 100, 90, 78, and 64 °C. The contour is the interpolation of observed or calculated values, and the number on the map is the linewidth (kHz).

FT spectrum at $\theta=\pi/2$ in Fig. 4 is similar in shape to that at small P in Fig. 7, which gives a hint on understanding the spin dynamics. In both cases there is a beat of oscillation in the signal, originating from many transition frequencies.

We observed FI signals by changing the above mentioned parameters. Figure 8 shows the contour map of the FT linewidth which becomes broader on increasing N_{Rb}, B_0, and θ ($<\pi/2$) values. In the case of large P, we can see a remarkable θ dependence of the linewidth. The width is nearly proportional to N_{Rb} at fixed B_0, θ, and P values. The B_0 dependence of the width at $P\sim 0.9$ ($I_P=1$ W) is larger than that at $P\sim 0.45$ ($I_P=0.19$ W). In particular, at $N_{\mathrm{Rb}}\sim 1.5\times 10^{12}$ cm^{-3}, $B_0\sim 10$ G, $P\sim 0.9$, and $\theta\sim\pi/2$, the line is slightly broader than that at $P\sim 0.45$. The spin-exchange interaction induces not only narrowing but also broadening for polarized atoms. On the other hand, the resonance lines of unpolarized atoms are broad and depend weakly on θ at any N_{Rb} and B_0 values.

IV. DISCUSSION

Figure 9 shows the FI profiles at various pulse areas, which were numerically calculated from the coupled equations (A11) and (A12), and are in good accordance with the observed signals shown in Fig. 3. The optically detected signals are proportional to the component $\langle S_y\rangle$ as explained by Eq. (B2), which can be obtained from the state multipole as shown in Eq. (C8). The components $\rho(FF)^1_Q$ ($F=2$ and 3, $Q=\pm 1$), which express the FI signals, are coupled with other components of $\Delta K=0,\pm 1$ and $\Delta Q=0,\pm 1$ by the spin-exchange interaction. After the spin temperature is raised by the rf pulse, the $Q=0$ components of ^{85}Rb and ^{87}Rb atoms decay to a new equilibrium together with phase relaxation of the ^{85}Rb atoms. Therefore, the FI signal and the

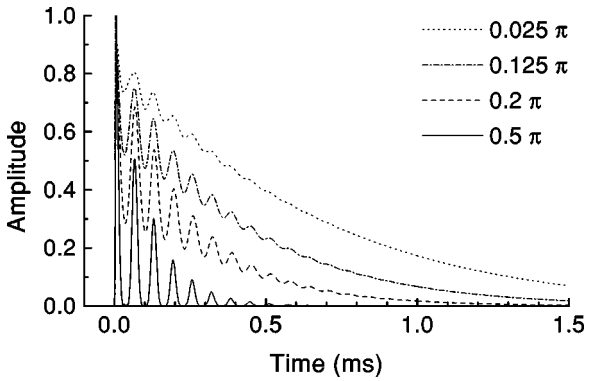

FIG. 9. The normalized FI profiles calculated at $T=110\,^{\circ}\mathrm{C}$, $B_0=10.5$ G, $P=0.9$, $\langle\sigma_{ex}\rangle=3.5\times10^{-18}$ m^2, $\langle\sigma_{SS}\rangle=5\times10^{-21}$ m^2, and $T_{NS}=10$ ms.

longitudinal relaxation should not be expressed by a single exponential decay, although other relaxation processes such as diffusion are negligible. However, we approximately fitted Lorentzian curves to the FT spectrum to obtain the linewidth.

The linewidths calculated at $P=0.9$ are fitted to the observed FT lines as shown in Fig. 10. There are three parameters to describe the spin interactions as mentioned in Appendix A: the cross section of the spin-exchange collision between Rb atoms $\langle\sigma_{ex}\rangle$, the spin relaxation collision between Rb atoms $\langle\sigma_{SS}\rangle$, and the spin-relaxation due to the buffer gas $\langle\sigma_{NS}\rangle$. The parameters obtained by the fitting are listed in Table I. The value of $\langle\sigma_{ex}\rangle$ is in accordance with that in Ref. [3], and much larger than the other cross sections. These parameters would become more accurate by reducing the error in N_{Rb} and the residual inhomogeneity of the magnetic field. When we set the value of $\langle\sigma_{ex}\rangle$ to zero in the calculation, the θ dependence of the linewidth disappears. Therefore, the observed spin dynamics is due to the spin-exchange interaction. As shown in Eqs. (A8) and (A10), $\langle\sigma_{SS}\rangle$ and $\langle\sigma_{NS}\rangle$ appear in a combination of the rate $1/T_{SS}+1/T_{NS}$, at which the state multipole ρ_1 relaxes to the $\varphi_1(F'F)^K_Q$ state. We explain here qualitatively the θ dependence at certain B_0 and P values. The obvious feature of the spin-exchange mainly comes from the second term of Eq. (A8), which at $\theta=\pi/2$ has no effect on the spin relaxation even at large P because the time average of $|\langle\mathbf{S}\rangle|$ becomes small because of the modulation at the splitting frequency of Zeeman transitions. Since the modulation frequency is proportional to the square of the magnetic field, the linewidth depends on B_0. This situation can be applied to the case of small P, where the spin of a colliding atom is in a random direction at any θ value, i.e., $|\langle\mathbf{S}\rangle|$ is small on the average.

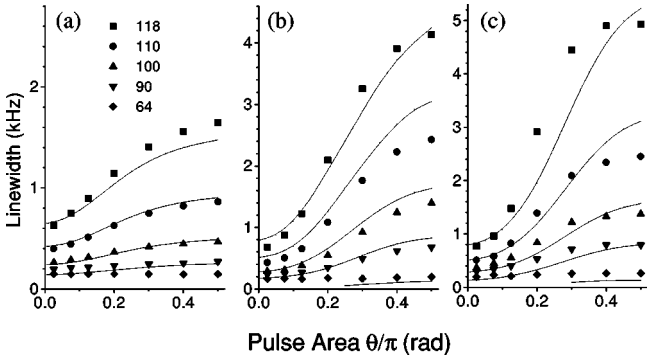

FIG. 10. The linewidth of FT spectra from the observed (dotted symbols) and calculated (solid lines) FI signals for several temperatures (°C). The magnetic field is (a) 0.21 G, (b) 5.1 G, and (c) 10.5 G. The parameters used in the calculation are $P=0.9$, $\langle\sigma_{ex}\rangle=3.5\times10^{-18}$ m^2, $\langle\sigma_{SS}\rangle=5\times10^{-21}$ m^2, and $T_{NS}=10$ ms. The line observed at low temperature is broadened by the inhomogeneous magnetic field.

TABLE I. The cross sections of spin interaction between Rb atoms. These were obtained by fitting the calculated linewidth to the observed one. $\langle N_{buf}v\,\sigma_{NS}\rangle$ was fixed at the averaged relaxation rate due to both buffer gases ^{4}He and N_2.

Cross section	(m^2)	Collision rate at 110 °C	(ms^{-1})
$\langle\sigma_{ex}\rangle$	3.5×10^{-18}	$N_{Rb}\langle v\rangle\langle\sigma_{ex}\rangle$	13.8
$\langle\sigma_{SS}\rangle$	5×10^{-21}	$N_{Rb}\langle v\rangle\langle\sigma_{SS}\rangle$	0.02
		$\langle N_{buf}v\,\sigma_{NS}\rangle$	0.1

Finally, we present the contour maps of calculated linewidth as the dashed line in Fig. 8. When the Larmor frequency is near the collision rate of spin exchange $1/T_{ex}$, as reported in Ref. [14], the line becomes narrow as the density increases [30]. In our case, however, the Larmor frequency is much larger than $1/T_{ex}\propto N_{Rb}$. Therefore, the contour lines are equidistant along the axis of N_{Rb}. The broadening at $\theta=\pi/2$ is more sensitive to the density N_{Rb} than that at $\theta\sim0$. Because the effective $|\langle\mathbf{S}\rangle|$ is small under the conditions of large magnetic field and small polarization, the spin relaxation can be quantitatively explained by the first term of Eq. (A8). By substituting Eq. (C4) into Eq. (A8), the relaxation rate is approximately equal to $(3/4)(1/T_{NS}+1/T_{SS}+1/T_{ex})\sim3/4T_{ex}$. The linewidth $3/4\pi T_{ex}=3.3$ kHz obtained from Table I agrees with the width at 10 G and 110 °C shown in Fig. 8. The observed and calculated contour maps are in good accordance with each other, but we can see a discrepancy between them at small P and large N_{Rb}. This is because the initial polarization by the weak pump was inhomogeneous in the cell under strong absorption, whereas FI profiles were calculated at a fixed polarization over the densities shown in Fig. 8.

V. CONCLUSION

We observed the FI signals of dense Rb atoms, and obtained the dependence of the decay rate on B_0, P, and θ. The experimental results were quantitatively interpreted as the intrinsic dynamics of highly polarized multilevel atoms under the influence of the spin-exchange interaction. The time evolution of atomic coherence was obtained by numerically integrating the nonlinear Liouville equation. The cross section of the spin-exchange collision, which was measured to be 3.5×10^{-18} m^2 by fitting the calculated dependence of the linewidth on B_0, P, θ, and N_{Rb}, is consistent with the previously reported values [3]. From this work we obtained the useful information, for example, of how to measure the

diffusion coefficient or magnetic resonance images. In such experiments, the small pulse area and strong polarization are reasonably suitable for dense alkali-metal atoms because the relaxation by spin-exchange collision becomes smaller than other physical processes.

The dense Rb atoms can be optically polarized by $P \sim 0.9$ at less than 120 °C with an injection-seeded high-power laser diode, and can be optically detected with the master laser. However, the light absorption is too strong to detect the FI signal at higher temperatures. We are planning to detect such signals by Faraday rotation of the probe light or magnetic detection by pickup coils, and to use a more powerful and narrower laser diode for pumping Rb atoms in a thin glass cell.

ACKNOWLEDGMENTS

This work was supported by the Saneyoshi Foundation, the Research Foundation for Opto-science and Technology, and a Grant-in-Aid for Scientific Research of Japan Society of the Promotion of Science.

APPENDIX A: LIOUVILLE EQUATION

Here we show an outline of the theory, reflecting on the experimental conditions. Our notation in this paper follows that used in Ref. [15]. When the alkali-metal atoms are free from collisions, the Hamiltonian of each atom in the ground state is [31]

$$H_0 = A\mathbf{I}\cdot\mathbf{S} + g_J\mu_B S_z B_0 + g_I\mu_B I_z B_0, \tag{A1}$$

where a static magnetic field B_0 is applied along the z axis, A is the constant of hyperfine coupling between the nuclear spin $\mathbf{I}$ and the electron spin $\mathbf{S}$, g_J is the g factor of the ground state electron, g_I is the g factor of the nuclear magnetic moment, and μ_B is the Bohr magneton. We treat the spin dynamics of the ground state by the state multipole $\rho(F'F)^K_Q$ of the density operator, which is the irreducible tensor of order K with $2K+1$ components, $Q=-K,\ldots,K$, and is related to the operator in the $|FM_F\rangle$ representation as follows [32–34]:

$$\rho(F'F)^K_Q = (-1)^{F'-M'}\sqrt{2K+1} \times \begin{pmatrix} F' & F & K \\ M' & -M & -Q \end{pmatrix} \rho(F'M',FM), \tag{A2}$$

where F' and F are the total angular momenta of the Rb atom, and the right hand side is summed over the axial components M' and M. If we optically pump the atoms sufficiently long to realize an equilibrium, the spin temperature is well defined to describe the population in the ground state [9,15,35]. Therefore, the nonzero components of the initial state are

$$\rho_0(FF)^K_0 = \frac{(-1)^{F-M}}{Z_I Z_S}\sqrt{2K+1}\begin{pmatrix} F & F & K \\ M & -M & 0 \end{pmatrix} e^{\beta M}, \tag{A3}$$

where β is the parameter of spin temperature, and Z_J is the partition function,

$$Z_J = \frac{\sinh[(2J+1)\beta/2]}{\sinh(\beta/2)}. \tag{A4}$$

The electron-spin polarization P is expressed using β as

$$P = \frac{\langle S_z\rangle}{S} = \tanh\left(\frac{\beta}{2}\right), \tag{A5}$$

where $\langle O\rangle$ is the trace $\mathrm{Tr}(\rho O)$. The initial components for the optically pumped atoms can be obtained from Eqs. (A3) and (A5) by giving the polarization P in the numerical calculation.

The pulse of rf magnetic field is applied after the optical pulse. The interaction Hamiltonian with the rf field is

$$H_1 = g_J\mu_B 2B_1 S_x \cos(\omega t), \tag{A6}$$

where $2B_1$ is the amplitude of the rf field oscillating along the x axis. The rf pulse makes the state multipole $\rho'(F'F)^K_Q$ nutate in the frame rotating at the angular frequency ω of the rf field. The spin relaxation is slow enough to be neglected during the rf pulse. When the pulse duration is sufficiently short, the bandwidth of the rf spectrum becomes much larger than the splittings of Zeeman frequencies. Therefore, the rf field is resonant with all the Zeeman transitions and the time evolution of the state multipole is a simple rotation as [34]

$$\rho'(F'F)^K_Q = \delta(F',F)e^{-i(\pi/2)Q}d^K_{Q0}(\Omega t)\rho_0(FF)^K_0, \tag{A7}$$

where $\delta(F',F)$ is the Kronecker delta function and $d^K_{QQ'}(\theta)$ is the reduced rotation matrix, $\Omega=\gamma B_1$, and γ is the gyromagnetic ratio of each hyperfine level. We applied a rf pulse whose duration is an integer multiple of the oscillation period, so $\rho(F'F)^K_Q = \rho'(F'F)^K_Q$ at the end of the pulse.

Next, we consider the spin interaction between alkali-metal atoms and buffer gas atoms. The mean collision rate of spin interaction is smaller than the Larmor frequency and larger than the spin relaxation rate in our experiment. Since the collision is instantaneous compared with the time evolution of free atoms in a magnetic field, the density operator ρ of colliding atoms i and j changes to $P_{ij}\rho P^\dagger_{ij}$ by a single collision of spin exchange, where $P_{ij} = 1/2 + 2\mathbf{S}_i\cdot\mathbf{S}_j$ [7]. The effect of collisions is introduced in the Liouville equation as the relaxation term. We use the rubidium atoms ^{85}Rb ($I=5/2$) and ^{87}Rb ($I=3/2$) in natural abundance. The former is resonant with the rf field, hereafter indicated by a subscript 1. The latter is off resonant and indicated by a subscript 2. For ^{85}Rb atoms, the spin interaction is expressed as [3,15]

$$R_1=(\varphi_1-\rho_1)\left(\frac{1}{T_{\rm NS}}+\frac{1}{T_{\rm SS}}+\frac{1}{T_{\rm ex}}\right)+\frac{4\varphi_1\langle\mathbf{S}_j\rangle\cdot\mathbf{S}_1}{T_{{\rm ex},1j}}, \tag{A8}$$

where the second term is summed over $j=1$ and 2, the rate $1/T_{\rm NS}$ shows the spin relaxation due to the buffer gases ^{4}He and N_2, $1/T_{\rm SS}=N_{\rm Rb}\langle v\sigma_{\rm SS}\rangle$ is the rate of spin relaxation due to the collisions between Rb atoms, v is the relative velocity of a colliding pair, and $\sigma_{\rm SS}$ is the cross section. We assume that $T_{\rm NS}$ and $T_{\rm SS}$ have the same values for both isotopes. $T_{\rm ex}$ is the collision time of the spin-exchange interaction, where $1/T_{\rm ex}=1/T_{{\rm ex},11}+1/T_{{\rm ex},12}$, $1/T_{{\rm ex},ij}=[{\rm A}_j]\langle v\sigma_{\rm ex}\rangle_{ij}$, $[{\rm A}_j]$ is the number density of atom ${\rm A}_j$, and $\sigma_{\rm ex}$ is the cross section. The operator φ_j is the part of the density operator without electron-spin polarization [15], and is expressed by

$$\varphi_j=\frac{1}{4}\rho_j+\mathbf{S}_j\cdot\rho_j\mathbf{S}_j. \tag{A9}$$

The initial polarization of ^{85}Rb atoms, expressed by the spin temperature, is reduced by the rf pulse to a new equilibrium including both ^{85}Rb and ^{87}Rb atoms coupled by the second term of Eq. (A8). For ^{87}Rb atoms the spin interaction is expressed as follows:

$$R_2=\left\{\frac{\langle S_{1z}\rangle}{T_{{\rm ex},21}}-\langle S_{2z}\rangle\left(\frac{1}{T_{\rm NS}}+\frac{1}{T_{\rm SS}}+\frac{1}{T_{{\rm ex},21}}\right)\right\}4\varphi_2 S_{2z}, \tag{A10}$$

where $\langle S_{2x}\rangle$ and $\langle S_{2y}\rangle$ are neglected because no sublevel coherence of ^{87}Rb atoms is induced by the rf field, and $\langle S_{1x}\rangle$ and $\langle S_{1y}\rangle$ are neglected because the polarization transfer of transverse components is ineffective between isotopes with different Larmor frequencies. From the detailed balance at equilibrium, $\langle v\sigma_{\rm ex}\rangle_{12}$ is equal to $\langle v\sigma_{\rm ex}\rangle_{21}$. If we assume that $\langle v\sigma_{\rm ex}\rangle_{11}=\langle v\sigma_{\rm ex}\rangle_{12}\equiv\langle v\sigma_{\rm ex}\rangle$, we may express $[^{85}{\rm Rb}]T_{{\rm ex},11}=[^{87}{\rm Rb}]T_{{\rm ex},12}=N_{\rm Rb}T_{\rm ex}$. The collision rate depends on the cell temperature through the number density of Rb atoms $N_{\rm Rb}$, the relative velocity v, and the cross section $\sigma_{\rm ex}$.

After the irradiation of the rf pulse, the density operator of ^{85}Rb atoms follows the Liouville equation,

$$\frac{d}{dt}\rho_1(F'F)^K_Q=\frac{1}{i\hbar}[H_0,\rho_1]+R_1. \tag{A11}$$

This is the ordinary differential equation system. There are included 144 independent components $\rho_1(F'F)^K_Q$. The irreducible components of the above-mentioned operators are obtained in Appendix C. The Hamiltonian H_0 mixes $\rho_1(F'F)^K_Q$ of $\Delta F=0,\pm1$, $\Delta K=0,\pm1$, and $\Delta Q=0$. The spin interaction R_1 nonlinearly mixes the components of $\Delta F=0,\pm1$, $\Delta K=0,\pm1$, and $\Delta Q=0,\pm1$. Therefore $\rho_1(F'F)^K_Q$ are coupled with each other, and all of them have to be calculated for ^{85}Rb atoms. On the other hand, the right hand side of Eq. (A10) is assumed to include only $Q=0$ components because the coherence that can be induced by the off-resonant rf pulse and the collision with ^{85}Rb atoms is negligible. Therefore we will succeed in solving the problem if we obtain only eight components for ^{87}Rb atoms,

$$\frac{d}{dt}\rho_2(FF)^K_0=R_2. \tag{A12}$$

Both Eqs. (A11) and (A12) are coupled with each other through the $\langle\mathbf{S}_j\rangle\cdot\mathbf{S}_i$ term of the spin-exchange interaction.

APPENDIX B: OPTICAL DETECTION

The probe beam of wavelength λ resonant with the D_1 line is circularly polarized and propagated along the y axis. We detect the transmission of probe light. The signal is proportional to the absorption cross section,

$$\sigma=\frac{8\pi^2\langle FM|\mu^\dagger|fm\rangle\langle fm|\mu|F'M'\rangle}{\varepsilon_0 h\lambda(\Delta_P+\Delta_L)}\rho(F'M',FM), \tag{B1}$$

where ε_0 is the dielectric constant in vacuum, and the right hand side is summed over F',M',F,M for the ground state and over f and m for the excited state. The buffer gas pressure is high enough to disturb the atomic coherence related to the excited state, and the Zeeman splitting is much smaller than the linewidths of the laser Δ_L and pressure broadening Δ_P. Therefore, we obtain

$$\sigma=\frac{\lambda^2}{2\pi}\frac{\Delta_N}{\Delta_P+\Delta_L}\left(\frac{1}{2}+\langle S_y\rangle\right), \tag{B2}$$

where the natural linewidth $\Delta_N=16\pi^3|\mu_{jJ}|^2/3\varepsilon_0 h\lambda^3$, μ_{jJ} is the reduced matrix element of the electric dipole moment, and j and J are the total electron angular momenta of the excited and ground states, respectively. We neglected high-frequency components because we are interested in the oscillation around the Larmor frequency. The optically detected signal is proportional to the component of the electron spin along the propagation of the probe beam, and is equivalent to the induced voltage of the pickup coil used in the usual magnetic resonance experiments.

APPENDIX C: CODING OF LIOUVILLE EQUATION AS IRREDUCIBLE TENSOR

We straightforwardly solved the nonlinearly coupled differential equations (A11) and (A12) by using the fourth-order Runge-Kutta method for numerical integration. Although we observed FI signals around Larmor frequencies less than 5 MHz, each step of the time evolution is set at 0.1 ns in the calculation, which is smaller than the period of phase rotation by hyperfine interaction. Since the differential equations are nonlinearly coupled through the spin-exchange interaction between Rb atoms, we cannot use the rotating wave approximation for the splitting frequency of the hyperfine levels. For example, it takes 4 h to calculate a FI signal of 1 ms duration under our circumstances (Pentium III 800 MHz and VISUAL C++).

We obtain here the irreducible components of the density operator (state multipole) and interaction operators used in the text. The density operator satisfies the following basic relation [32–34]:

$$\sum_F \sqrt{2F+1}\rho(F,F)_0^0=\sum_{FM} \rho(FM,FM)=1, \qquad \text{(C1)}$$

when all atoms are in the ground state and the number of atoms is conserved. By using Eq. (C1) and the symmetry of the state multipole, we tested the accuracy of the results obtained numerically.

The time evolution of the state multipole is described by the Liouville equation,

$$i\hbar\frac{d}{dt}\rho(F'F)_Q^K=\sum_{F''K'Q'K''Q''}(-1)^{Q+F+F'}\times\sqrt{(2K+1)(2K'+1)(2K''+1)}\times\begin{pmatrix} K' & K'' & K\\ -Q' & -Q'' & Q\end{pmatrix}\begin{Bmatrix} K' & K'' & K\\ F & F' & F''\end{Bmatrix}\times[H(F'F'')_{Q'}^{K'}\rho(F''F)_{Q''}^{K''}-\rho(F'F'')_{Q'}^{K'}H(F''F)_{Q''}^{K''}], \qquad \text{(C2)}$$

where ( ) means the 3-j symbol, and { } the 6-j symbol for the coupling of angular momenta.

The Hamiltonian of free atoms is well known in the $|FM_F\rangle$ representation. Therefore the irreducible components can be obtained by the same relation as Eq. (A2),

$$\begin{aligned}H_0(F'F)_Q^K&=\sum_{M'M}(-1)^{F'-M'}\sqrt{2K+1}\begin{pmatrix} F' & K & F\\ -M' & Q & M\end{pmatrix}H_0(F'M',FM)\\&=\delta(F',F)\delta(K,0)\delta(Q,0)\sqrt{2F+1}\frac{A}{2\hbar}[F(F+1)-J(J+1)-I(I+1)]\\&\quad+\delta(K,1)\delta(Q,0)g_J\mu_B\frac{B_0}{\sqrt{3}\hbar}(-1)^{I+J+1+F'}\sqrt{J(J+1)(2J+1)(2F+1)(2F'+1)}\begin{Bmatrix} F' & F & 1\\ J & J & I\end{Bmatrix}\\&\quad+\delta(K,1)\delta(Q,0)g_I\mu_B\frac{B_0}{\sqrt{3}\hbar}(-1)^{I+J+1+F}\sqrt{I(I+1)(2I+1)(2F+1)(2F'+1)}\begin{Bmatrix} F' & F & 1\\ I & I & J\end{Bmatrix}, \qquad \text{(C3)}\end{aligned}$$

where we substitute J for S as the ground state of the alkali-metal atoms. The first term is the hyperfine interaction which is diagonal for F and the monopole ($K=0$). The second and third terms are, respectively, the Zeeman interactions of electron and nuclear spin, which mix the components $\rho(F'F)_Q^K$ of $\Delta F=0,\pm1$, $\Delta K=0,\pm1$, and $\Delta Q=0$. We should not neglect the mixing of $\Delta K=\pm1$ by the magnetic field, because the mixing leads to the splitting of Zeeman transitions and the observed linewidth depends on the magnetic field.

For spin relaxation by buffer gas collision $\langle\sigma_{NS}\rangle$ and collision with alkali-metal atoms $\langle\sigma_{SS}\rangle$, the state multipole relaxes to the state φ_j depending only on the nuclear-spin parameter [15]. From Eq. (A9),

$$\begin{aligned}\varphi_j(F'F)_Q^K&=\frac{1}{4}\rho_j(F'F)_Q^K\\&\quad-\sum_{F''F'''}(-1)^{F'+F''+K}J(J+1)(2J+1)\times\sqrt{(2F+1)(2F'+1)(2F''+1)(2F'''+1)}\times\begin{Bmatrix} F''' & F'' & K\\ F' & F & 1\end{Bmatrix}\begin{Bmatrix} F' & F'' & 1\\ J & J & I\end{Bmatrix}\begin{Bmatrix} F''' & F & 1\\ J & J & I\end{Bmatrix}\\&\quad\times\rho_j(F''F''')_Q^K, \qquad \text{(C4)}\end{aligned}$$

and φ_j is a linear combination of the state multipole. We should take account of all components for ^{85}Rb atoms, and some of the components $\varphi_2(F'F)_{Q=0}^K$ for ^{87}Rb atoms.

For the spin-exchange interaction $\langle\sigma_{\rm ex}\rangle$, the second term of Eq. (A8) can be positive or negative according to the relative direction of electron spins in the colliding atoms. The following are the results after many calculations:

$$\begin{aligned}(\langle\mathbf{S}_1\rangle\cdot\mathbf{S}_1)(F'F)_Q^K&=\sum_{F''F'''}\delta(K,1)\times(-1)^{F'+F''}\frac{J(J+1)(2J+1)}{3}\times\sqrt{(2F+1)(2F'+1)(2F''+1)(2F'''+1)}\times\begin{Bmatrix} F'' & F''' & 1\\ J & J & I\end{Bmatrix}\begin{Bmatrix} F' & F & 1\\ J & J & I\end{Bmatrix}\\&\quad\times\rho_1(F''F''')_Q^1, \qquad \text{(C5)}\end{aligned}$$

$$(4\varphi_1\langle \mathbf{S}_1\rangle\cdot\mathbf{S}_1)(F'F)^K_Q=\sum_{K'Q'K''Q''F''}\begin{pmatrix}K'' & K' & K\\ Q'' & Q' & -Q\end{pmatrix}\begin{Bmatrix}K'' & K' & K\\ F' & F & F''\end{Bmatrix}(-1)^{F'-F-Q}$$
$$\times\sqrt{(2K+1)(2K'+1)(2K''+1)}\,4\varphi_1(F'F'')^{K'}_{Q'}(\langle \mathbf{S}_1\rangle\cdot\mathbf{S}_1)(F''F)^{K''}_{Q''}, \quad \text{(C6)}$$

$$(4\varphi_j S_{jz})(F'F)^K_Q=\sum_{K'F''}\begin{pmatrix}1 & K' & K\\ 0 & Q & -Q\end{pmatrix}\begin{Bmatrix}1 & K' & K\\ F' & F & F''\end{Bmatrix}\begin{Bmatrix}F'' & F & 1\\ J & J & I\end{Bmatrix}$$
$$\times(-1)^{F'-F+F''-Q+J+I+1}\sqrt{(2K+1)(2K'+1)J(J+1)(2J+1)(2F+1)(2F''+1)}\,4\varphi_j(F'F'')^{K'}_Q\,. \quad \text{(C7)}$$

For ^{85}Rb atoms, Eq. (A8) and Eqs. (C3)–(C7) are substituted into Eq. (A11). For ^{87}Rb atoms, the $Q=0$ components of Eqs. (A10), (C4), and (C7) are substituted into Eq. (A12). Both sets of equations are nonlinear differential equation systems. When we detect the resonance signal induced by a weak rf field, the analytical solution can be obtained by the approximation of using the linear terms. However, we apply a rf $\pi/2$ pulse in the experiment, so we cannot neglect the higher order of the density operator.

The optically detected signal is oscillating in proportion to $\langle S_y\rangle$ as shown in Eq. (B2). Because sublevel coherence is induced for ^{85}Rb atoms, the component around the Larmor frequency is

$$\langle S_y\rangle=\frac{i}{\sqrt{6}}\sum_F(-1)^{F+J-I}(2F+1)\sqrt{J(J+1)(2J+1)}$$
$$\times\begin{Bmatrix}F & 1 & F\\ J & I & J\end{Bmatrix}[\rho_1(FF)^1_{-1}+\rho_1(FF)^1_1]. \quad \text{(C8)}$$

[1] T. G. Walker and W. Happer, Rev. Mod. Phys. **69**, 629 (1997).
[2] D. F. Phillips, A. Fleischhauer, A. Mair, R. L. Walsworth, and M. D. Lukin, Phys. Rev. Lett. **86**, 783 (2001).
[3] W. Happer, Rev. Mod. Phys. **44**, 169 (1972).
[4] H. G. Dehmelt, Phys. Rev. **105**, 1487 (1957).
[5] F. A. Franz and E. Lüscher, Phys. Rev. **135**, A582 (1964).
[6] F. A. Franz and C. E. Sooriamoorthi, Phys. Rev. A **8**, 2390 (1973).
[7] F. Grossetête, J. Phys. (Paris) **25**, 383 (1964).
[8] F. Grossetête, J. Phys. (Paris) **29**, 456 (1968).
[9] L. W. Anderson, F. M. Pipkin, and J. C. Baird, Phys. Rev. **116**, 87 (1959).
[10] S. Appelt, A. Ben-Amar Baranga, A. R. Young, and W. Happer, Phys. Rev. A **59**, 2078 (1999).
[11] K. Ishikawa, S. Morii, K. Enomoto, and T. Yabuzaki, J. Opt. Soc. Am. B **17**, 182 (2000).
[12] C. J. Erickson, D. Levron, W. Happer, S. Kadlecek, B. Chann, L. W. Anderson, and T. G. Walker, Phys. Rev. Lett. **85**, 4237 (2000).
[13] S. Kadlecek, L. W. Anderson, C. J. Erickson, and T. G. Walker, Phys. Rev. A **64**, 052717 (2001).
[14] W. Happer and H. Tang, Phys. Rev. Lett. **31**, 273 (1973).
[15] S. Appelt, A. Ben-Amar Baranga, C. J. Erickson, M. V. Romalis, A. R. Young, and W. Happer, Phys. Rev. A **58**, 1412 (1998).
[16] K. Ishikawa and T. Yabuzaki, Phys. Rev. A **62**, 065401 (2000).
[17] M. P. Gorza, S. Saltiel, H. Failache, and M. Ducloy, Eur. Phys. J. D **15**, 113 (2001).
[18] K. Ishikawa, K. Iida, and T. Nakura, Phys. Rev. A **63**, 013405 (2001).
[19] F. J. Duarte, *Tunable Lasers Handbook* (Academic Press, London, 1995).
[20] D. Cassettari and E. Arimondo, Opt. Lett. **23**, 1135 (1998).
[21] J. N. Zerger, M. J. Lim, K. P. Coulter, and T. E. Chupp, Appl. Phys. Lett. **76**, 1798 (2000).
[22] I. A. Nelson, B. Chann, and T. G. Walker, Appl. Phys. Lett. **76**, 1356 (2000).
[23] B. Chann, I. Nelson, and T. G. Walker, Opt. Lett. **25**, 1352 (2000).
[24] M. Merimaa, H. Talvitie, P. Laakkonen, M. Kuittinen, I. Tittonen, and E. Ikonen, Opt. Commun. **174**, 175 (2000).
[25] W. Nagengast and K. Rith, Opt. Lett. **22**, 1250 (1997).
[26] M. V. Romalis, Appl. Phys. Lett. **77**, 1080 (2000).
[27] Coherent Inc. S-79-2000C-150-H. The typical output power was 0.7 W at a current of 1.2 A and temperature of 30 °C, and 1 W in free running.
[28] SDL Inc. 2382-P1. The typical output power with seed light was 3 W at a current of 5.4 A and temperature of 9 °C. The same power was obtained in free running.
[29] A. N. Nesmeyanov, *Vapor Pressure of the Chemical Elements* (Elsevier, Amsterdam, 1963).
[30] A frequency chirp of the FI signal is predicted by our calculation of large P and Larmor frequency near $1/T_{ex}$, because the frequency depends on the polarization P under these conditions.
[31] E. Arimondo, M. Inguscio, and P. Violino, Rev. Mod. Phys. **49**, 31 (1977).
[32] B. W. Shore, *The Theory of Coherent Atomic Excitation* (John Wiley & Sons, New York, 1990).
[33] K. Blum, *Density Matrix Theory and Applications* (Plenum, New York, 1981).
[34] D. M. Brink and G. R. Satchler, *Angular Momentum* (Oxford University Press, New York, 1993).
[35] A. Javan, Phys. Rev. Lett. **3**, 87 (1959).